# Spatiotemporal evolution of Poiseuille-Rayleigh-Bénard flows in binary fluids with Soret effect under initial pulselike disturbances

J. Hu,[1,*] X. Y. Yin,[2] D. Henry,[3] and H. Ben Hadid[3]
[1]*Institute of Applied Physics and Computational Mathematics, P.O. Box 8009, Beijing 100088, China*
[2]*Department of Modern Mechanics, University of Science and Technology of China, Hefei 230027, China*
[3]*Laboratoire de Mécanique des Fluides et d'Acoustique, CNRS–Université de Lyon–Ecole Centrale de Lyon–Université Lyon 1–INSA de Lyon, ECL, 36 Avenue Guy de Collongue, 69134 Ecully Cedex, France*
(Received 13 March 2009; revised manuscript received 22 June 2009; published 20 August 2009)

The spatiotemporal evolution of Poiseuille-Rayleigh-Bénard flows in binary fluids with Soret effect is investigated by carrying out fully nonlinear two-dimensional numerical simulations initiated by a pulselike disturbance. The traveling wave packets for positive as well as negative separation factors $\psi$ are obtained numerically for ethanol-water-like mixtures (Prandtl number Pr=10, Lewis number Le=0.01) and selected combinations of Rayleigh and Reynolds numbers at $\psi$=0.01, 0.1 and $\psi$=−0.1. The characteristics of the wave fronts and the transitions observed between absolute and convective instabilities when changing the parameters are compared with the results previously obtained by linear spatiotemporal stability analysis. The simulations are in very good agreement with the stability results, which confirms the validity of both approaches. Finally, in order to characterize the possible interaction between the two wave packets of the so-called downstream and upstream modes for $\psi<0$, the spatiotemporal stability analysis is used to detect a boundary curve in the (Re, Ra) parameter region beyond which the two wave packets will never completely separate. Numerical simulations illustrate the different evolutions of the wave packets on both sides of this boundary.

DOI: 10.1103/PhysRevE.80.026312 PACS number(s): 47.20.Bp, 47.60.Dx

## I. INTRODUCTION

Mixed convection in binary mixtures with Soret effect has many practical applications, such as chemical vapor deposition (CVD) in the electronics industry. It also leads to a variety of spatiotemporal patterns, the study of which has a great theoretical interest. In fact, the spatiotemporal behavior of the dissipative structures appearing in binary mixture convection [1] is already complex due to the combination of thermal forcing (characterized by the Rayleigh number Ra) and Soret coupling between temperature and concentration fields (characterized by the separation factor $\psi$), and the externally imposed throughflow will add a new influence.

Jung *et al.* [2] were the first to investigate how a horizontal plane Poiseuille shear flow changes linear convection properties in binary fluid layers heated from below. They solved the full linear stability equations by a shooting method for realistic top and bottom boundary conditions. For negative Soret coupling, they elucidated the throughflow lifting of the Hopf symmetry degeneracy of left and right traveling waves (TW). They also showed how the frequencies, bifurcation thresholds, and structural properties of the two TW solution branches—as well as the stationary overturning convection (SOC)—were dramatically changed when a throughflow was applied. Later, Büchel, and Lücke [3] investigated the effect of a horizontal Poiseuille throughflow on stationary and traveling wave convective patterns which appear for negative Soret coupling. The numerical calculations in a two-dimensional periodic box containing two counterrotating near-critical transverse rolls are performed with a Galerkin expansion or a finite-difference numerical method. Bifurcation diagrams of various quantities such as Nusselt number, frequency, and mixing behavior are determined as functions of heating rate and wave number for several throughflow rates and Soret coupling strengths for ethanol-water parameters. They also studied the growth dynamics of small convective perturbations into different, strongly nonlinear convective states and the transition between them. Concerning the characterization of the absolute or convective nature of the instabilities in such flows, the boundary curves separating these two types of instabilities for both negative separation factors (corresponding to the two TW solutions) and positive separation factors (corresponding to the SOC solution) are first plotted as a function of the throughflow rate in the paper of Jung *et al.* [2] Büchel and Lücke [4] then studied the linear spatiotemporal properties of spatially localized convective perturbations for heated binary fluid layers, with or without throughflow. Fronts and pulselike wave packets formed out of the three relevant perturbations (two oscillatory ones and a stationary one) are analyzed after evaluating the appropriate saddle points of the three respective dispersion relations of the linear stability equations over the complex wave number plane. Some comparisons with pulses and fronts obtained by numerical simulation are also given. Finally, Jung and Lücke [5] investigated the nonlinear evolution of traveling wave fronts and localized traveling wave convection in binary fluid mixtures with strongly negative Soret coupling. They used numerical simulations performed in two-dimensional long-extent cavities to point out and elucidate the differences in the evolutions of fronts and localized waves.

By using the Chebyshev collocation method to solve the full linear stability equations, Hu *et al.* [6] further investigated the temporal and spatiotemporal instabilities of the Poiseuille-Rayleigh-Bénard flows for much larger Reynolds numbers. For positive separation factors, they found that the critical thresholds strongly increase when the throughflow is

*Corresponding author: hu_jun@iapcm.ac.cn

 

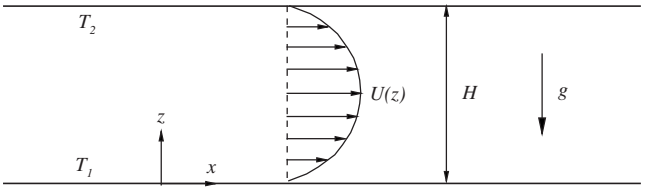


FIG. 1. Schematic of the Poiseuille-Rayleigh-Bénard model.

applied, and the boundary curves between absolute and convective instabilities (AI/CI) increase as well, but more steeply. For enough large positive separation factors, there exist three local minima in the neutral curves (Rayleigh number against wave number) for moderate Reynolds numbers, which results in the discontinuity of the critical wave number curve and the nonsmoothness of the critical Rayleigh number curve when the Reynolds number is varied. For negative separation factors, there exists a contact point between the critical Rayleigh number curve and the AI/CI boundary curve at which the fluid system makes a direct transition from stable to absolutely unstable without crossing the convectively unstable region.

In this paper, the spatiotemporal evolution of Poiseuille-Rayleigh-Bénard flows is numerically investigated in a long-extent two-dimensional cavity by introducing a pulselike initial velocity perturbation. The numerical simulations are chosen to illustrate and analyze specific behaviors revealed by the linear spatiotemporal stability analysis. Our two-dimensional analysis implies that we consider convection rolls with axes oriented transversally, i.e., perpendicular to the throughflow direction. Such flow structures are those obtained in channels that are narrow in the transverse direction, and our two-dimensional approximation, although it does not take into account the variations in the transverse direction, can efficiently describe these structures. Other flow structures, as longitudinal rolls with axes oriented parallel to the flow, which can be obtained in wider channels, will have different bifurcation thresholds and different behaviors, but they cannot be described by our two-dimensional model. The paper is organized as follows. The formulation of the problem is given in Sec. II, and the mixed finite element method adopted for the numerical simulations is presented in Sec. III. In Sec. IV, the spatiotemporal simulations of Poiseuille-Rayleigh-Bénard flows for positive and negative separation factors are presented and analyzed, and we present our conclusion in Sec. V.

## II. FORMULATION OF THE PROBLEM

We consider a nonreactive binary fluid mixture contained in a two-dimensional horizontal channel of height $H$ (Fig. 1). The binary mixture is heated from below: the horizontal boundaries are isothermal and held at different temperatures, $T_2$ at the top wall ($z=H$) and $T_1 > T_2$ at the bottom wall ($z=0$). A throughflow is also generated in the $x$ direction by imposing a constant pressure gradient along the channel. The resulting global flow is usually called the Poiseuille-Rayleigh-Bénard flow.

Due to the influence of gravity, the binary mixture may become unstable when vertical temperature and concentration gradients exist. To take this into account, the density variations are considered, but according to the Boussinesq approximation, they are restricted to the buoyancy term and are expressed as a linear law,

$$\rho = \rho_0[1 - \beta_T(T - T_0) - \beta_C(C - C_0)], \tag{1}$$

where $\beta_T$ and $\beta_C$ are the thermal and solutal expansion coefficients; $\rho_0$, $T_0$, and $C_0$ are reference values for density, temperature, and concentration, respectively, which are taken as the mean initial values of the respective fields.

The Soret effect, which arises as the contribution of the temperature gradient to the mass flux, is considered here, whereas the Dufour effect, which arises as the contribution of the concentration gradient to the heat flux, is neglected. This assumption is valid for liquid mixtures. The mass flux $J_C$ and the heat flux $J_T$ are then

$$J_C = -\rho_0 D_C \nabla C - \rho_0 D_S \nabla T, \tag{2a}$$

$$J_T = -D_T \nabla T, \tag{2b}$$

where $D_C$, $D_S$, and $D_T$ are the solutal diffusion coefficient, Soret diffusion coefficient, and thermal conductivity, respectively. The conductive steady state will then correspond to linear variations along the vertical $z$ direction for both the temperature and the concentration, leading to a concentration difference $\Delta C = -D_S \Delta T / D_C$ induced by the applied temperature difference $\Delta T = T_1 - T_2$.

The flow in this system is modeled by the Navier-Stokes equations coupled to an energy equation and a concentration equation. In these equations, length, velocity, time, and pressure are scaled by $H$, $\kappa/H$, $H^2/\kappa$, and $\rho_0 \kappa^2/H^2$, respectively ($\kappa$ is the thermal diffusivity). The dimensionless temperature $\theta$ and concentration $c$ are defined as $(T-T_0)/\Delta T$ and $(C-C_0)/\Delta C$. Thus the dimensionless governing equations of the two-dimensional Poiseuille-Rayleigh-Bénard flow are

$$\nabla \cdot \mathbf{v} = 0, \tag{3a}$$

$$\frac{\partial \mathbf{v}}{\partial t} + \mathbf{v} \cdot \nabla \mathbf{v} = -\nabla p + \mathrm{Pr} \nabla^2 \mathbf{v} + \mathrm{Ra}\,\mathrm{Pr}(\theta + \psi c)\mathbf{e}_z, \tag{3b}$$

$$\frac{\partial \theta}{\partial t} + \mathbf{v} \cdot \nabla \theta = \nabla^2 \theta, \tag{3c}$$

$$\frac{\partial c}{\partial t} + \mathbf{v} \cdot \nabla c = \mathrm{Le}(\nabla^2 c - \nabla^2 \theta), \tag{3d}$$

where $\mathbf{v} = (u, w)$ is the two-dimensional dimensionless velocity vector, $\mathbf{e}_z$ is the unit vector in the vertical direction, and the operators are defined as $\nabla = (\partial_x, \partial_z)$ and $\nabla^2 = \partial_x^2 + \partial_z^2$. The dimensionless parameters appearing in the governing system [Eq. (3)] are the Prandtl number, $\mathrm{Pr} = \nu/\kappa$, the Rayleigh number, $\mathrm{Ra} = \beta_T g H^3 \Delta T / \kappa \nu$, the separation factor, $\psi = -\beta_C D_S / \beta_T D_C$, and the Lewis number, $\mathrm{Le} = D_C / \kappa$. Here, $\nu$ is the kinematic viscosity. The corresponding boundary conditions are

$$\text{no-slip conditions:} \quad u = w = 0, \quad \text{at} \quad z = 0,1, \tag{4a}$$

$$\text{thermal conditions:} \quad \theta = 0.5, \quad \text{at} \quad z = 0, \tag{4b}$$

$$\theta = -0.5, \quad \text{at} \quad z = 1, \tag{4c}$$

$$\text{mass impermeability:} \quad \partial_z \theta - \partial_z c = 0, \quad \text{at} \quad z = 0,1. \tag{4d}$$

The nondimensional basic steady state can easily be obtained and corresponds to a parabolic $z$ profile for the $x$ component of the velocity vector (throughflow), to linear conductive $z$ profiles for temperature and concentration, and to a pressure gradient which is constant in the throughflow direction and linear in $z$ in the vertical direction (gravitational effects):

$$\bar{u}(z) = -6 \ \mathrm{Re} \ \mathrm{Pr}(z^2 - z), \tag{5a}$$

$$\nabla \bar{p} = -12 \ \mathrm{Re} \ \mathrm{Pr}^2 \mathbf{e}_x + \mathrm{Ra} \ \mathrm{Pr}(1 + \psi)(0.5 - z)\mathbf{e}_z. \tag{5b}$$

$$\bar{\theta}(z) = 0.5 - z, \tag{5c}$$

$$\bar{c}(z) = 0.5 - z. \tag{5d}$$

Here, $\mathrm{Re} = U_0 H/\nu$ is the Reynolds number, and $U_0$ is the dimensional mean velocity obtained by integration over the channel width.

The disturbed two-dimensional Poiseuille-Rayleigh-Bénard flow with Soret effect can be decomposed as $u = \bar{u} + u'$, $w = w'$, $p = \bar{p} + p'$, $\theta = \bar{\theta} + \theta'$, and $c = \bar{c} + c'$. The perturbation equations are then represented as

$$\nabla \cdot \mathbf{v}' = 0, \tag{6a}$$

$$\frac{\partial u'}{\partial t} + \mathbf{v}' \cdot \nabla u' + \bar{u}\frac{\partial u'}{\partial x} + \frac{d\bar{u}}{dz} w' = -\frac{\partial p'}{\partial x} + \mathrm{Pr}\nabla^2 u', \tag{6b}$$

$$\frac{\partial w'}{\partial t} + \mathbf{v}' \cdot \nabla w' + \bar{u}\frac{\partial w'}{\partial x} = -\frac{\partial p'}{\partial z} + \mathrm{Pr}\nabla^2 w' + \mathrm{Ra} \ \mathrm{Pr}(\theta' + \psi c'), \tag{6c}$$

$$\frac{\partial \theta'}{\partial t} + \mathbf{v}' \cdot \nabla \theta' + \bar{u}\frac{\partial \theta'}{\partial x} - w' = \nabla^2 \theta', \tag{6d}$$

$$\frac{\partial c'}{\partial t} + \mathbf{v}' \cdot \nabla c' + \bar{u}\frac{\partial c'}{\partial x} - w' = \mathrm{Le}(\nabla^2 c' - \nabla^2 \theta'). \tag{6e}$$

Here, $\mathbf{v}' = (u', w')$. The corresponding boundary conditions are

$$\text{no-slip conditions:} \quad u' = w' = 0, \quad \text{at} \quad z = 0,1, \tag{7a}$$

$$\text{thermal conditions:} \quad \theta' = 0, \quad \text{at} \quad z = 0,1, \tag{7b}$$

$$\text{mass impermeability:} \quad \partial_z \theta' - \partial_z c' = 0, \quad \text{at} \quad z = 0,1. \tag{7c}$$

It is these perturbation equations which we will solve in the two-dimensional channel. In the numerical simulations, the channel will be long, but of finite length $L$, in the $x$ direction and we will impose periodic boundary conditions in this direction for all the perturbation variables.

## III. MIXED FINITE ELEMENT METHOD

A quadrilateral mesh is used for the computations and the variables in each element are expanded in Galerkin basis functions,

$$u' = \sum_{i=1}^{9} u_i'(t)\phi^i, \quad w' = \sum_{i=1}^{9} w_i'(t)\phi^i, \quad \theta' = \sum_{i=1}^{9} \theta_i'(t)\phi^i,$$
$$c' = \sum_{i=1}^{9} c_i'(t)\phi^i, \quad p' = \sum_{i=1}^{4} p_i'(t)\varphi^i, \tag{8}$$

where $\phi^i$ and $\varphi^i$ are biquadratic and bilinear basis functions (Taylor-Hood elements) which satisfy the well-known Babuška-Brezzi condition [7]. The spurious node-to-node oscillations appearing for finite Reynolds numbers are then avoided. The usual Galerkin approach (orthogonality in the basis function space) allows to replace the governing Eq. (6) by the following continuity $R_C^i$, momentum $R_M^i$, energy $R_E^i$ and solute $R_S^i$ residual equations:

$$R_C^i = \int_V \nabla \cdot \mathbf{v}' \varphi^i dV = 0, \tag{9a}$$

$$R_M^i = \int_V \left[ \frac{\partial \mathbf{v}'}{\partial t} + \mathbf{v}' \cdot \nabla \mathbf{v}' + \bar{u}\frac{\partial \mathbf{v}'}{\partial x} + \frac{d\bar{u}}{dz} w' \mathbf{e}_x - \mathrm{Pr}\nabla \cdot \mathbf{T} - \mathrm{Ra} \ \mathrm{Pr}(\theta' + \psi c')\mathbf{e}_z \right] \phi^i dV = 0, \tag{9b}$$

$$R_E^i = \int_V \left[ \frac{\partial \theta'}{\partial t} + \mathbf{v}' \cdot \nabla \theta' + \bar{u}\frac{\partial \theta'}{\partial x} - w' - \nabla^2 \theta' \right] \phi^i dV = 0, \tag{9c}$$

$$R_S^i = \int_V \left[ \frac{\partial c'}{\partial t} + \mathbf{v}' \cdot \nabla c' + \bar{u}\frac{\partial c'}{\partial x} - w' - \mathrm{Le}(\nabla^2 c' - \nabla^2 \theta') \right] \phi^i dV = 0, \tag{9d}$$

where $\mathbf{T} = -p'\mathbf{I}/\mathrm{Pr} + [\nabla \mathbf{v}' + (\nabla \mathbf{v}')^{\mathrm{T}}]$.

At the top and bottom walls, the essential boundary conditions (7a) and (7b) are applied for the streamwise and vertical velocities and for the temperature, while the natural boundary conditions (7c) are used for the concentration. We also impose periodic boundary conditions in the $x$ direction.

The residuals $R_C^i$, $R_M^i$, $R_E^i$, and $R_S^i$ are evaluated numerically using nine-point Gaussian integration. The residual equation (9), which correspond to a system of nonlinear algebraic equations, are solved with the Newton-Raphson iterative method,

$$\mathbf{q}^{(n+1)} = \mathbf{q}^{(n)} - \mathbf{J}^{-1}\mathbf{R}(\mathbf{q}^{(n)}), \quad \mathbf{J} = \frac{\partial \mathbf{R}}{\partial \mathbf{q}}. \tag{10}$$

Here, $\mathbf{q}^{\mathrm{T}}=[u_1', w_1', \theta_1', c_1', p_1', \cdots, u_N', w_N', \theta_N', c_N', p_N']$ is the vector of the unknowns and $\mathbf{J}$ is the Jacobian matrix of the residuals $\mathbf{R}$ with respect to the nodal unknowns $\mathbf{q}$. At each Newton-Raphson step, a system of linear equations characterized by a banded matrix is obtained, which is solved by the ILUTC-GMRES iterative method [8]. For the stationary problem, the Newton-Raphson method may be used directly to converge to a stationary state of the flow system, while for the transient problem, the Crank-Nicolson scheme is used for time integration and the Newton-Raphson method is used at each time step. Numerical accuracy has been tested by doubling the number of finite elements in both $x$ and $z$ directions and by reducing the time step by half. All the results presented in this study have been checked to remain visually indistinguishable from those obtained with a higher discretization, and are thus considered mesh and time step independent.

## IV. RESULTS OF THE SPATIOTEMPORAL NUMERICAL SIMULATIONS

In order to validate the finite element approach presented in the previous section, preliminary numerical simulations of two-dimensional PRB flows of binary fluids with Soret effect have been carried out by two of the present authors [9]. The calculations were performed in a periodic region of length $L=2$ for Pr=10, Le=0.01, $\psi=0.1$, Re=0.1 and several values of the Rayleigh number. They were initiated by a temperature perturbation applied at an arbitrary position, as done by Büchel and Lücke [4]. The results for Ra=2000 show that only the mode with the wave number $k_r=\pi$ is initially amplified whereas all the other modes are damped. There is then a continuous growth of the $k_r=\pi$ mode until nonlinear effects become important. After a nonlinear transition, the flow finally evolves into a periodic right traveling wave. Similar results are obtained for Ra=1000, 1500, and 2500. The computed linear temporal growth rates and phase velocities are in very good agreement with those obtained from the linear stability equations [6], indicating that the mixed finite element code is well adapted for PRB flow simulations. In the following, we will use this code to study the convective/absolute stability properties of the PRB flows and we will compare our results with those already obtained by a linear stability approach [6]. Note that the computations will be performed for fixed values of the Prandtl and Lewis numbers (Pr=10, Le=0.01).

Following the method used by Delbende and Chomaz [10] a divergence-free velocity disturbance $\mathbf{v}'(x,z,t=0)$ is used as the initial velocity field. This disturbance is defined by

$$u' = -(z-z_0)\exp\left[-\left(\frac{(x-x_0)^2}{2\sigma_x^2} + \frac{(z-z_0)^2}{2\sigma_z^2}\right)\right], \tag{11a}$$

$$w' = \frac{\sigma_z^2}{\sigma_x^2}(x-x_0)\exp\left[-\left(\frac{(x-x_0)^2}{2\sigma_x^2} + \frac{(z-z_0)^2}{2\sigma_z^2}\right)\right]. \tag{11b}$$

It corresponds to a Gaussian pulselike perturbation which is located at ($x=x_0$, $z=z_0$) and has a typical extent $\sigma_x$ along the $x$ direction and $\sigma_z$ along the $z$ direction. The length scales $\sigma_x$ and $\sigma_z$ must *a priori* be taken as small as possible. Nevertheless, in order to keep enough spectral information with all physically relevant wave numbers, we choose $\sigma_x=\sigma_z=0.1$. This initial perturbation is in fact a small vorticity spot.

This perturbation is expected to initiate a wave packet which will be convected inside the cavity. The numerical simulation will follow the evolution of this wave packet and determine its characteristics. The evolution of the wave packet at the linear stage can also be obtained by linear stability analysis using the absolute/convective instability theory. Let us recall some basic ideas. First, a wave packet will be amplified only if the system is unstable, i.e., in a state beyond the critical curve for the onset of instabilities. Then, if the amplifying wave packet is convected away from its initial position, the system is said to be convectively unstable. If, otherwise, the amplification can be observed locally, the system is said to be absolutely unstable. The AI/CI boundary curve indicates the boundary between these two regimes. Finally, for an amplifying wave packet, more precisions on its spatial evolution can be obtained by the AI/CI theory through the calculation of the propagation speeds of its left and right fronts [see Eqs. (12)–(14) of Ref. [6] presenting the calculation of the absolute growth rate in a moving frame].

### A. Positive separation factors ($\psi>0$)

#### 1. $\psi=0.01$

Let us first recall the results obtained by linear stability analysis for $\psi=0.01$. These results (extracted from Fig. 16 of Ref. [6]) are shown in Fig. 2 where are plotted together in the Re-Ra plane the critical curve for the onset of the instabilities (stable/unstable or S/U boundary curve) and the boundary curve between absolute and convective instabilities (AI/CI boundary curve). We can see that the Re-Ra plane is divided into three regions: the stable region, the convectively unstable region and the absolutely unstable region. There is generally a convectively unstable region between the stable and absolutely unstable regions, but a direct transition from the stable region to the absolutely unstable region is sometimes possible, as is the case for Re=0 in the situation at $\psi=0.01$. Different numerical simulations will be performed for $\psi=0.01$ at selected values of the parameters Re and Ra. The corresponding points in the Re-Ra plane are indicated by crosses ($\times$) in Fig. 2 and labeled from 1 to 4. The precise localization of these points is given in Table I, together with information obtained by linear stability analysis such as the stability properties and the propagation speeds of the left and right fronts of the amplifying wave packets. For each simulation, a periodic cavity of length $L=24$ or $L=32$ has been simulated and the initial perturbation is located at ($x_0=7$, $z_0=0.5$).

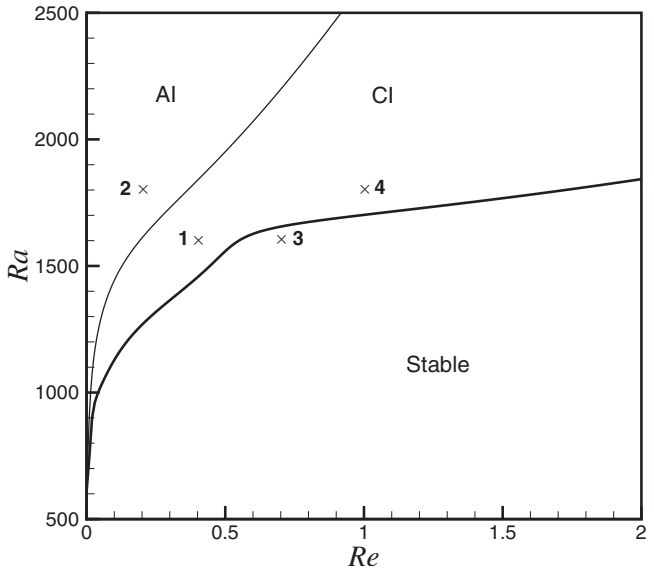


FIG. 2. Critical curve (stable/unstable transition, thick curve) and AI/CI boundary curve (thin curve) in the Re-Ra plane for PRB flows with Soret effect and $\psi=0.01$. Crosses (×) indicate parameter values at which numerical simulations are performed (see Table I and Fig. 3).

The spatiotemporal evolution of the perturbation is illustrated in Fig. 3 for the four selected cases. In each case, the vertical component of the velocity perturbation along the horizontal center line of the channel (shown as $w'$ profiles along $x$) is plotted at regularly spaced times in an $x$-$t$ graph. In all cases, the $w'$ signal appears very quickly as a periodic signal of wavelength close to 2, indicating that the mode with a wave number close to $k_r=\pi$ has been initially amplified whereas the other modes have been damped, in agreement with the critical wave numbers found in the temporal stability analysis. The results obtained in the different cases are now briefly described.

(i) Case 1: for this case [Fig. 3(a)], we see that the pulselike perturbations spread convectively downstream. The selected $k_r=\pi$ mode is continuously amplified, but quite slowly. The flow for this case is then convectively unstable, in good agreement with the results obtained by the linear AI/CI theory and shown in Fig. 2 and Table I.

TABLE I. Characteristics of the different cases ([indicated by crosses (×) in Fig. 2] for which a numerical simulation is performed for $\psi=0.01$ (Fig. 3): values of the Reynolds and Rayleigh numbers; stability properties [stable (S), convectively unstable (CI), absolutely unstable (AI)]; propagation speeds $V_l(V_r)$ of the left (right) fronts of the amplifying wave packets obtained from the linear AI/CI theory.

| Case | 1 | 2 | 3 | 4 |
|---|---|---|---|---|
| Re | 0.4 | 0.2 | 0.7 | 1.0 |
| Ra | 1600 | 1800 | 1600 | 1800 |
| S/CI/AI | CI | AI | S | CI |
| $V_l$ | 3.433 | −2.333 | / | 9.499 |
| $V_r$ | 7.673 | 7.678 | / | 17.082 |

(ii) Case 2: in this case [Fig. 3(b)], the perturbation grows much faster and locally, i.e., around its initial position. This is characteristic of an absolute instability, which also agrees with the prediction of the AI/CI theory.

(iii) Case 3: for this case which is below the critical curve, the perturbation is convected downstream with a decreasing amplitude, i.e., even the initially amplified $k_r=\pi$ mode is finally damped [Fig. 3(c)]. The flow in this case is then clearly stable.

(iv) Case 4: in this case [Fig. 3(d)], the perturbations spread convectively downstream as in case 1 indicating that the flows are convectively unstable. The perturbations, however, have larger growth rates and larger downstream velocities.

Note finally that, for each unstable case, the spatiotemporal rays, $x/t=V$, based on the propagation speeds of the left and right wave packet fronts obtained by the linear AI/CI theory, are in very good agreement with the numerically obtained wave packet evolution (Fig. 3).

### 2. $\psi=0.1$

According to the linear theory, for large enough positive separation factors (such as $\psi=0.1$), there exists a Reynolds number range where there is a transition between two different critical modes [6]. The neutral curves (Rayleigh number against wave number) in this Re range are plotted in Fig. 4 for $\psi=0.1$, reproducing Fig. 4(a) of Ref. [6]. We can see clearly that when Re=1.5 there is only one minimum at $k_r=2.88$ on the neutral curve. When increasing the Reynolds number, another local minimum first appears at a larger wave number ($k_r=3.97$ for Re=1.54), and then for Re≥1.6, a third local minimum appears at an intermediate wave number ($k_r=3.02$ for Re=1.6). For Re beyond 1.6, three local minima then exist on each neutral curve. The evolution of these minima with Re leads to a change of critical mode at Re=1.64 (between the low wave number minimum and the intermediate wave number minimum), inducing a discontinuity in the critical wave number curve and the nonsmoothness of the critical Rayleigh number curve. These phenomena were first mentioned in our linear stability analysis paper [6]. To better understand the dynamics of the wave packets in this Re range, we will consider two cases, the first one (Re=1.56) where the neutral curve has two minima and the second one (Re=1.64) where the neutral curve has three minima, and choose in each case a value of Ra slightly above the critical curve, respectively Ra=1400 and Ra=1500.

For Re=1.56 and Ra=1400 (values shown, respectively, by a heavy solid curve and a dashed line in Fig. 4), we first present the temporal growth rates ($\omega_i$) as a function of the real wave number ($k_r$) (result obtained by linear temporal stability analysis) in Fig. 5(a) and the local growth rates ($\omega_i^v$) as a function of the observer velocity $V=x/t$ (result obtained by the linear AI/CI analysis) in Fig. 5(b). We see that there exist two maximum temporal growth rates $\omega_{i,\max}$ at different wave numbers $k_r\approx 2.43$ and $k_r\approx 4.27$, and two maximum local growth rates $\omega_{i,\max}^v$ corresponding to different moving frame velocities $V\approx 20.64$ and $V\approx 24.52$ and belonging to different unstable branches. The branch with larger maximum growth rate and smaller wave number will be referred

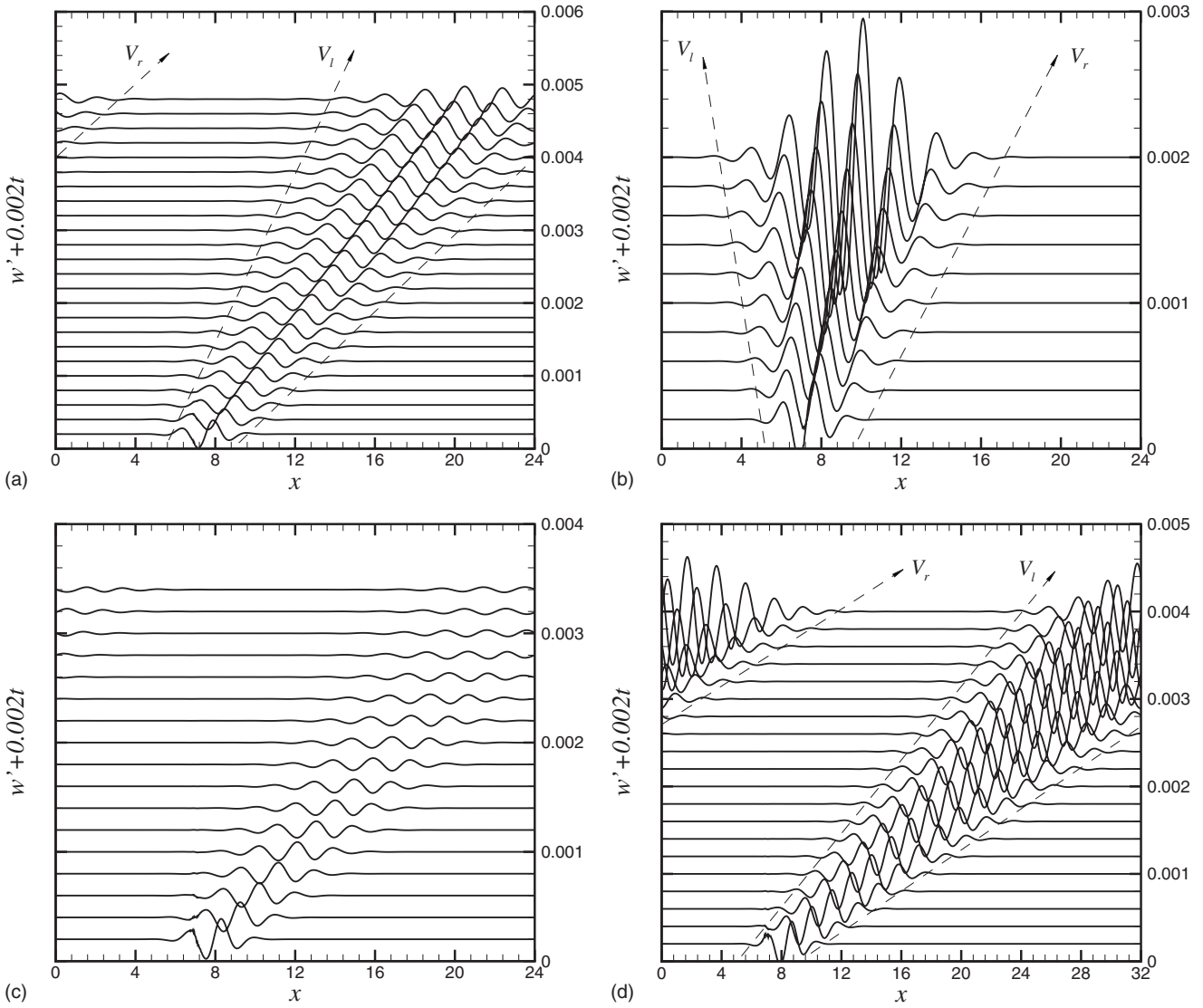


FIG. 3. Spatiotemporal evolutions generated by an initial pulselike velocity perturbation located at ($x_0$=7, $z_0$=0.5) in a PRB flow with Soret effect for four cases corresponding to selected (Re, Ra) pairs (see Table I and Fig. 2) and $\psi$=0.01: (a) Case 1; (b) Case 2; (c) Case 3; (d) Case 4. The vertical component of the velocity perturbation $w'$ along the center line of the channel is plotted at regularly spaced times. In each case, the $x$ range plotted corresponds to the size of the periodic cavity. For each amplifying wave packet, the spatiotemporal ray labeled $V_l(V_r)$ is based on the propagation speed of its left (right) front obtained by the linear AI/CI theory and given in Table I.

to as "branch I," and the other branch with smaller maximum growth rate and larger wave number as "branch II" [Fig. 5(a)]. For these two branches, the two wave front velocities can also be obtained [Fig. 5(b)]: they are $V_l$=20.077 and $V_r$=21.393 for branch I and $V_l$=24.306 and $V_r$=24.741 for branch II, $V_l$ concerning the left front and $V_r$ the right front. All this indicates that branch II has a faster downstream velocity than branch I, whereas branch I has a larger unstable region than branch II.

A numerical simulation has been performed for this case (Re=1.56, Ra=1400) inside a periodic cavity of length $L$ =40 and with an initial perturbation located at ($x_0$=7, $z_0$ =0.5). The spatiotemporal evolution of the $w'$ profile along the center line of the channel is shown in Fig. 6. Initially, the two branches overlap and up to $t$=0.8 only one wave packet can be seen [Fig. 6(a)]. For larger times ($1<t<3$) the two branches with different wavelengths can be gradually distinguished [Figs. 6(b) and 6(c)]. Finally, for $t \geq 3.5$ [Fig. 6(d)], the main parts of the two unstable branches are clearly separated. Note that a damping effect can be observed in the transition process from the initial wave packet to the two wave packets corresponding to branch I and branch II. This damping effect, which also takes place in the intermediate zone between the two wave packets, is a consequence of the negative temporal growth rates found for $3<k_r<3.8$ [see Fig. 5(a)]. The whole disturbed region can be bounded by two rays in the $x$-$t$ plane, one at the left front of branch I and the other at the right front of branch II. A good fit is obtained by choosing the front velocities obtained by the AI/CI theory ($V_l$=20.077 for branch I and $V_r$=24.741 for branch II), which indicates a very good agreement with the results obtained by spatiotemporal instability analysis [Fig. 5(b)]. The spatiotemporal patterns (temperature perturbation contours) at $t$=1.8 and $t$=3.5 are finally presented in Fig. 7. We clearly

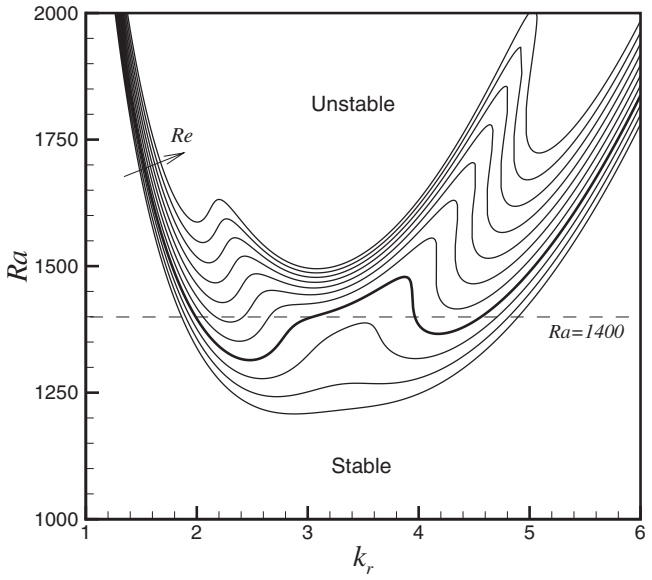


FIG. 4. Neutral curves (Rayleigh number Ra against real wave number $k_r$) for different Reynolds numbers, Re=1.5+$n\times$0.02 for $n$=0 to 10, and $\psi$=0.1. The arrow indicates increasing Re. The heavy solid curve corresponds to Re=1.56 and the dashed line to Ra=1400.

see the separation of the two wave packets corresponding to branch I and branch II, their different spatial extents and different wavelengths. Aside from these differences, note that the temperature patterns look very similar for the two branches.

A similar study is now performed for Re=1.64 and Ra =1500. The temporal growth rates ($\omega_i$) and the local growth rates ($\omega_i^v$) are given for this case in Fig. 8. From the two subfigures, it can be seen that there exist three maximum growth rates, two positive (unstable modes) and one negative (stable mode). The spatiotemporal approach [Fig. 8(b)] indicates that the three maximum growth rates belong to three different branches. Branch I and branch II have already been defined in the previous case (Re=1.56, Ra=1400). The new branch which corresponds to intermediate wave numbers is denoted by "branch III." We see that branch III has the largest growth rate, but also that its local growth rate curve has a large extent and completely covers the local growth rate curves of branch I and branch II. It can then be expected that branch III will dominate the whole spatiotemporal evolution in this case.

The numerical simulation performed in this case (Re =1.64, Ra=1500) has the same characteristics as in the previous case ($L$=40, $x_0$=7, $z_0$=0.5). The spatiotemporal evolution of the $w'$ profile along the center line of the channel is shown in Fig. 9, together with the spatiotemporal rays corresponding to the left and right front velocities obtained by the AI/CI theory for branch III. As expected, a single wave packet is obtained during the spatiotemporal evolution. Moreover, the spatiotemporal rays associated with the left and right front velocities of branch III well describe the spreading of the unstable wave packet. All this confirms the dominant influence of branch III.

In the two previous spatiotemporal simulations, we found that the time evolution of the left and right boundaries of the global wave packets can be well estimated by front velocities obtained by the spatiotemporal instability analysis. In fact, at the boundaries of the unstable wave packets, the disturbance amplitudes are small, which explains that the linear theory can predict the spreading velocity of these boundaries. In the central region of the wave packet, however, the wavelengths and temporal growth rates may deviate from the values obtained by the linear theory. For instance, for the first case (Re=1.56, Ra=1400), we know from our linear stability

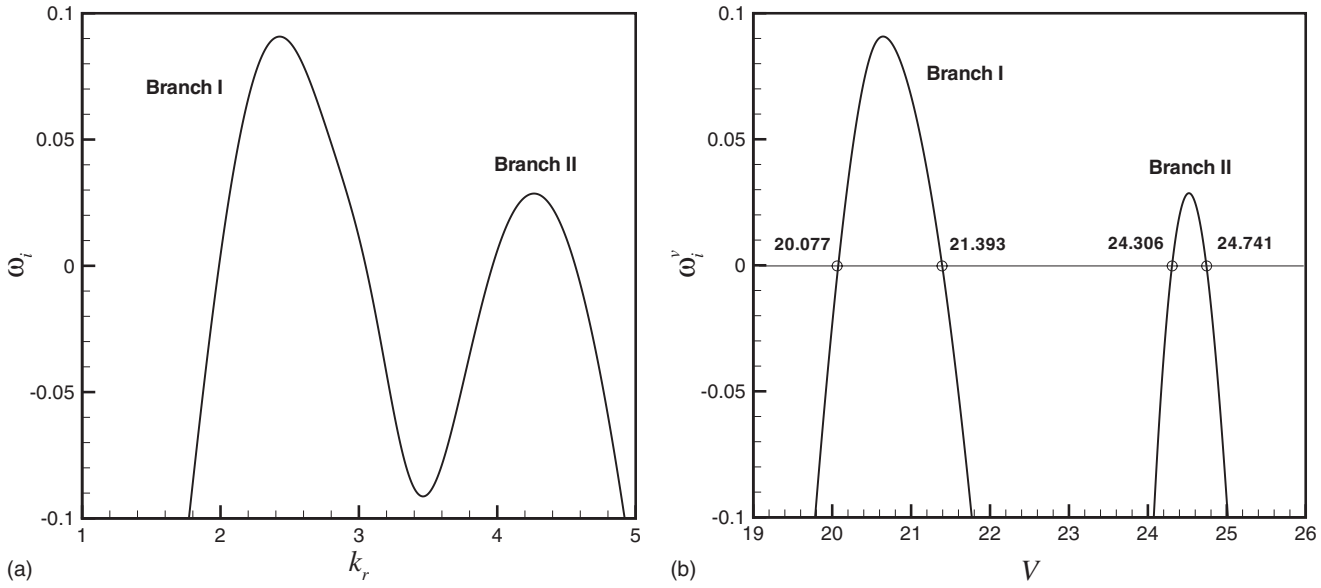


FIG. 5. (a) Temporal growth rates $\omega_i$ as a function of the real wave number $k_r$ (result obtained by temporal stability analysis) and (b) local growth rates $\omega_i^v$ as a function of the observer velocity $V=x/t$ (result obtained by spatiotemporal stability analysis) for the unstable branches I and II of the PRB flow with Soret effect for Re=1.56, Ra=1400, and $\psi$=0.1. In (b), the values of the left and right wave front velocities are given for each branch.

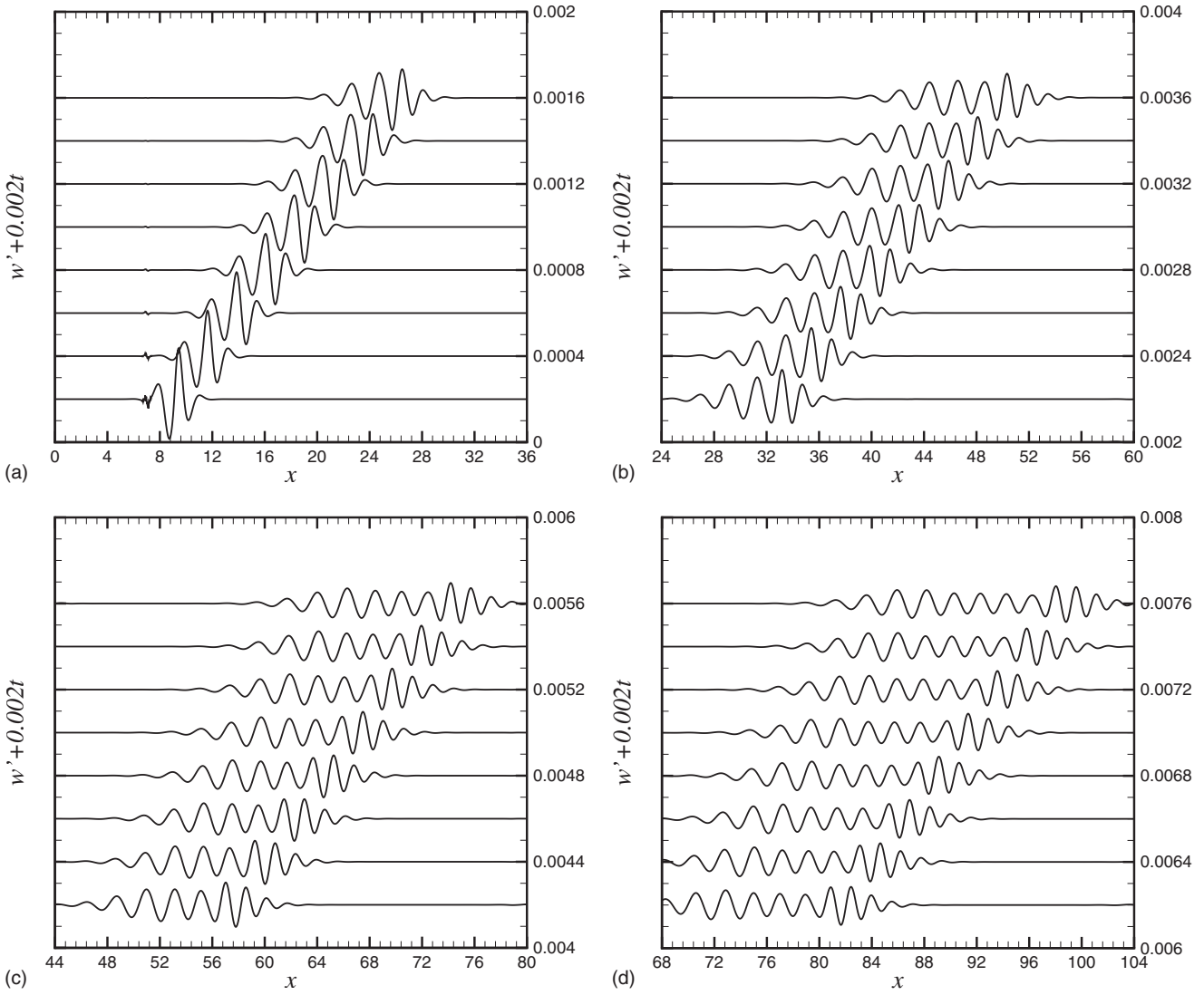


FIG. 6. Spatiotemporal evolution generated by an initial pulselike velocity perturbation located at ($x_0$=7, $z_0$=0.5) in a PRB flow with Soret effect for Re=1.56, Ra=1400, and $\psi$=0.1. The vertical component of the velocity perturbation $w'$ along the center line of the channel is plotted at regularly spaced times ($\Delta t$=0.1): (a) $t$=0.1–0.8; (b) $t$=1.1–1.8; (c) $t$=2.1–2.8; (d) $t$=3.1–3.8.

analysis that the wavelength of the unstable wave packet corresponding to the maximum growth rate for branch I should be $\lambda_m$=2.58 [Fig. 5(a)]; but the wavelength found for branch I from the simulation results at $t$=3.5, near the maximum amplitude of the signal, is smaller, about 2.3 [see the patterns in Fig. 7(b)]. For branch II which has a smaller maximum growth rate, it is found that the theoretical and simulated values for the spatial wavelength at maximum

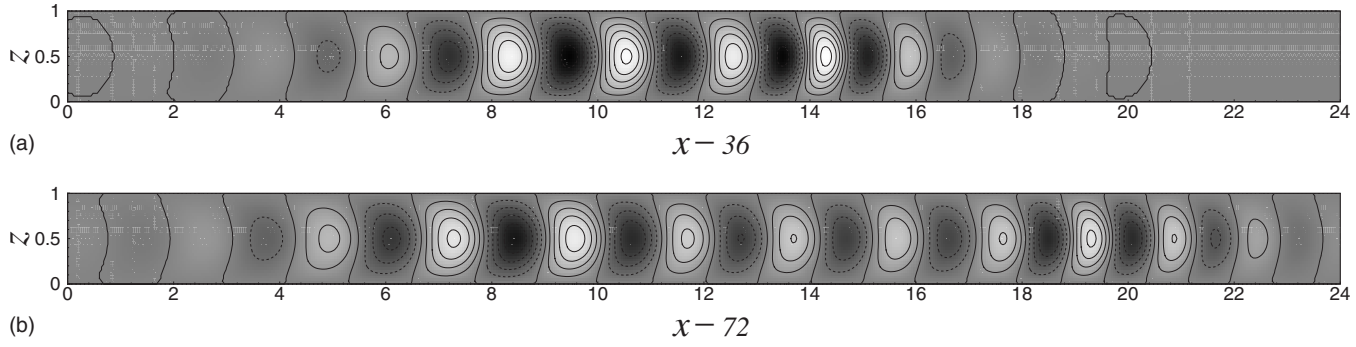


FIG. 7. Spatiotemporal patterns (temperature perturbation contours) obtained at (a) $t$=1.8 and (b) $t$=3.5 in a perturbed PRB flow with Soret effect for Re=1.56, Ra=1400, and $\psi$=0.1 (same case as in Fig. 6).

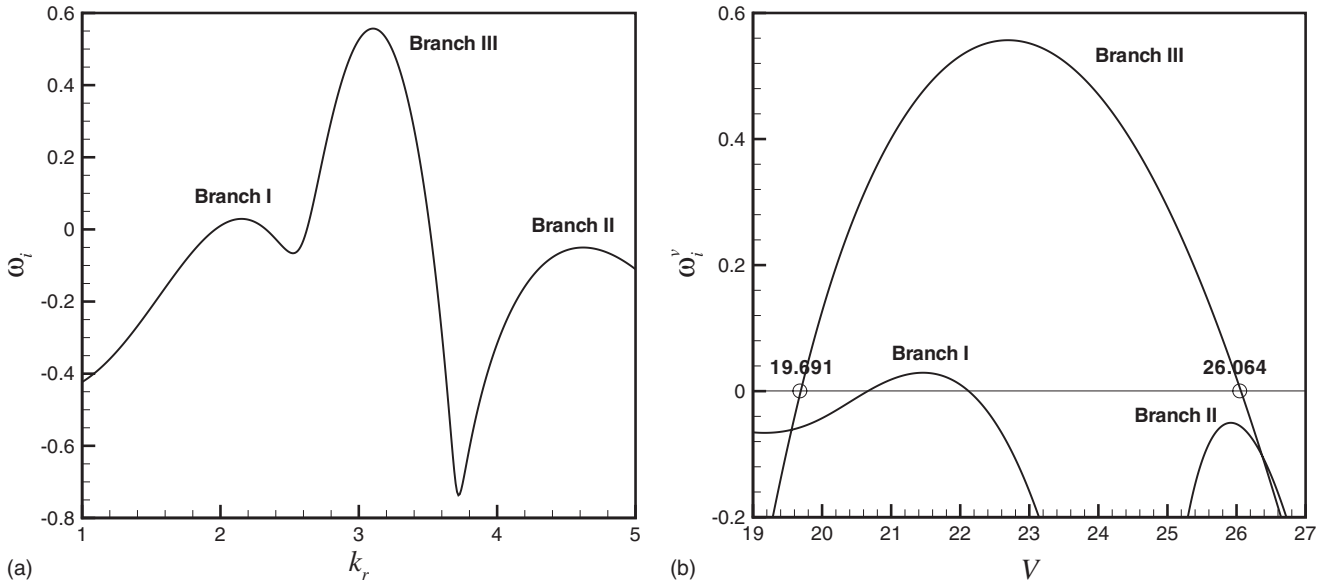


FIG. 8. (a) Temporal growth rates $\omega_i$ as a function of the real wave number $k_r$ (result obtained by temporal stability analysis) and (b) local growth rates $\omega_i^v$ as a function of the observer velocity $V=x/t$ (result obtained by spatiotemporal stability analysis) for the near-unstable branches I, II, and III of the PRB flow with Soret effect for Re=1.64, Ra=1500, and $\psi=0.1$. In (b), the values of the left and right wave front velocities are given for the dominant branch III.

temporal growth rate are 1.47 and 1.59, respectively. The difference is smaller than for branch I, but the smaller value is now the theoretical value. In fact, we can note that the computed values are between the two theoretical values. These differences between the theoretical and computed values could then be due to the fact that the two waves in the calculations are not yet separate and that there is an interaction between them. We can also argue that the wave packets may be changed by weak nonlinear effects because the selected situation is somewhat above the critical curve.

### B. Negative separation factors ($\psi<0$)

For negative separation factors, it is already known [2] that the throughflow lifts the Hopf symmetry degeneracy of left (upstream) and right (downstream) traveling waves (TW), generating two TW branches with different frequencies, bifurcation thresholds, and structural properties. The modes on these two branches will be named upstream (downstream) modes with reference to the negative (positive) value of the pulsation characterizing the branch in the

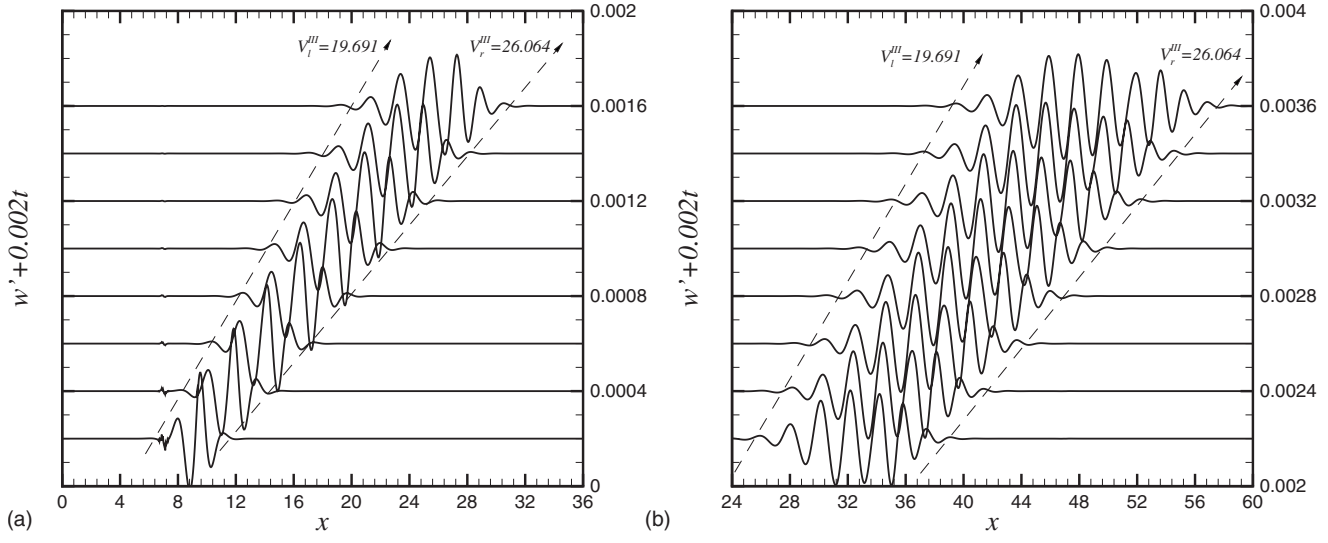


FIG. 9. Spatiotemporal evolution generated by an initial pulselike velocity perturbation located at ($x_0=7$, $z_0=0.5$) in a PRB flow with Soret effect for Re=1.64, Ra=1500, and $\psi=0.1$. The vertical component of the velocity perturbation $w'$ along the center line of the channel is plotted at regularly spaced times ($\Delta t=0.1$): (a) $t=0.1-0.8$; (b) $t=1.1-1.8$. The amplifying wave packet is bordered by the spatiotemporal rays associated with the left and right front velocities of branch III and obtained by the linear AI/CI theory.

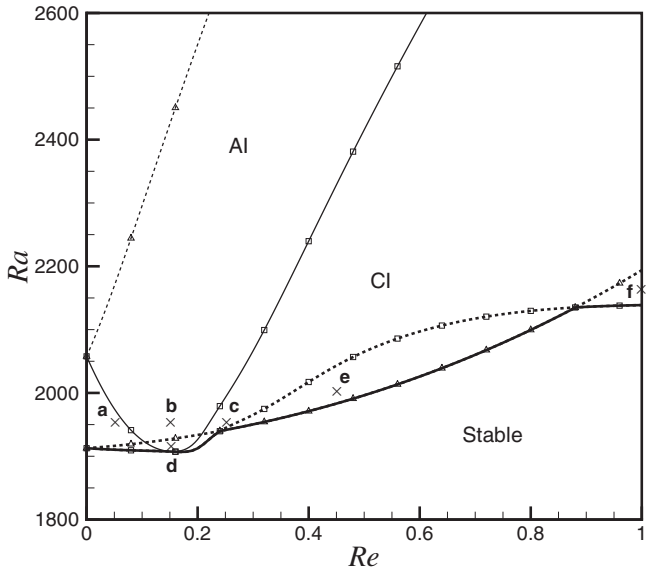


FIG. 10. Critical curves (stable/unstable transitions, thick curves) and AI/CI boundary curves (thin curves) in the Re-Ra plane for PRB flows with Soret effect and $\psi=-0.1$. The squares ($\square$) refer to the upstream modes, the triangles ($\triangle$) refer to the downstream modes, and the solid thick curve gives the true minimum critical Rayleigh number. Crosses ($\times$) indicate parameter values at which numerical simulations are performed (see Table II and Fig. 11).

limit $\mathrm{Re}\to 0$, and the associated traveling waves will be denoted by TWU (TWD).

The AI/CI boundary curves and critical curves for $\psi=-0.1$ are plotted in the Re-Ra plane in Fig. 10. In this figure, the squares ($\square$) refer to the upstream modes, the triangles ($\triangle$) refer to the downstream modes, the thin curves are the AI/CI boundary curves, the thick curves are the critical curves, and the solid thick curve gives the true minimum critical Rayleigh number. When increasing Re from zero, the critical Rayleigh number is first determined by the upstream mode, then the downstream mode becomes the critical mode in an intermediate range of Re, and finally, for larger Re, the upstream mode is again the critical mode. There also exists a contact point between the critical curve and the AI/CI boundary curve, at which the fluid system is directly changed from stable to absolutely unstable without crossing the convectively unstable region. According to these features, we select six representative situations, corresponding to (Re, Ra) pairs denoted by crosses ($\times$) in Fig. 10 and labeled from a to f. More details on these situations are given in Table II. For these six cases, a numerical simulation will be performed.

The spatiotemporal evolution of the perturbation [initially imposed at $(x_0, z_0)$] is illustrated in Fig. 11 for the six selected cases through the usual $w'$ profiles. For cases a, b, and c, a periodic cavity of length $L=24$ has been simulated, whereas for cases d, e, and f, $L=32$. The results obtained in the different cases are now described.

(i) Case a ($x_0=10$, $z_0=0.5$): in this case [Fig. 11(a)], the left and right wave packets, respectively, spread upstream and downstream, i.e., the front velocities verify $V_l^u<V_r^u<0$ and $V_r^d>V_l^d>0$. The flow is then convectively unstable, which agrees with the result found by linear spatiotemporal stability analysis.

(ii) Case b ($x_0=7$, $z_0=0.5$): from Fig. 11(b), it can be seen that the left wave packet of the upstream mode grows locally around its initial position, i.e., $V_l^u<0$ and $V_r^u>0$, which indicates an absolute instability, while the wave packet of the downstream mode spreads downstream, with larger front velocities than for case a, which indicates a convective instability. All this agrees with the linear stability results and confirms that in this case the whole flow system is absolutely unstable.

(iii) Case c ($x_0=4$, $z_0=0.5$): in this case [Fig. 11(c)], the left and right wave packets both spread downstream with different front velocities ($V_r^d>V_l^d>V_r^u>V_l^u>0$). So the flow is convectively unstable as for case a, but the upstream mode now spreads downstream. This phenomenon is in agreement with the linear spatiotemporal stability analysis, and confirms that the point c is within the convectively unstable parameter region as shown in Fig. 10.

(iv) Case d ($x_0=7$, $z_0=0.5$): from Fig. 11(d), it can be seen that the wave packet of the upstream mode grows locally around its initial position similarly to the case b ($V_l^u<0$ and $V_r^u>0$). For the downstream mode, however, the wave packet spreads downstream but with a damped amplitude. Thus, the downstream mode is stable, but due to the absolute instability of the upstream mode, the flow system is absolutely unstable. This also agrees with the spatiotemporal stability analysis, as shown in Table II and Fig. 10 for point d.

(v) Cases e and f ($x_0=4$, $z_0=0.5$). For these two cases [Figs. 11(e) and 11(f)], both left and right wave packets spread downstream. But for the case e, the wave packet for the upstream mode is damped whereas for the case f, it is the wave packet for the downstream mode which is damped.

TABLE II. Characteristics of the different cases [indicated by crosses ($\times$) in Fig. 10] for which a numerical simulation is performed for $\psi=-0.1$ (Fig. 11): values of the Reynolds and Rayleigh numbers; stability properties [stable (S), convectively unstable (CI), absolutely unstable (AI)] with respect to the traveling waves of the upstream mode (TWU), the downstream mode (TWD), both modes together (all TW).

| Case | a | b | c | d | e | f |
|---|---|---|---|---|---|---|
| Re | 0.05 | 0.15 | 0.25 | 0.15 | 0.45 | 1.0 |
| Ra | 1950 | 1950 | 1950 | 1910 | 2000 | 2160 |
| S/CI/AI (TWU) | CI | AI | CI | AI | S | CI |
| S/CI/AI (TWD) | CI | CI | CI | S | CI | S |
| S/CI/AI (all TW) | CI | AI | CI | AI | CI | CI |

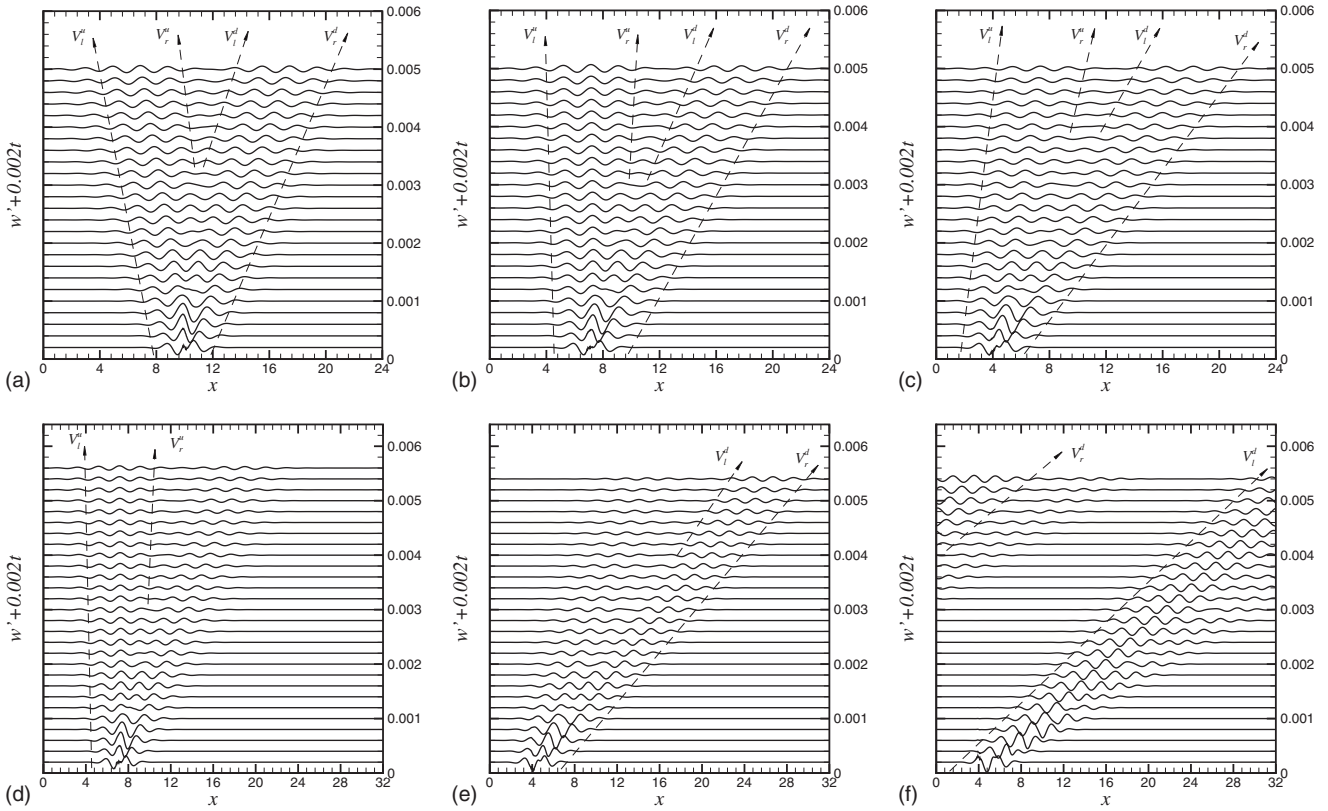


FIG. 11. Spatiotemporal evolutions generated by an initial pulselike velocity perturbation located at $(x_0, z_0=0.5)$ in a PRB flow with Soret effect for six cases corresponding to selected (Re, Ra) pairs (see Table II and Fig. 10) and $\psi=-0.1$: (a) Case a ($x_0=10$); (b) Case b ($x_0=7$); (c) Case c ($x_0=4$); (d) Case d ($x_0=7$); (e) Case e ($x_0=4$); (f) Case f ($x_0=4$). The vertical component of the velocity perturbation $w'$ along the center line of the channel is plotted at regularly spaced times. In each case, the $x$ range plotted corresponds to the size of the periodic cavity. For each amplifying wave packet, the spatiotemporal ray labeled $V_l(V_r)$ is based on the propagation speed of its left (right) front obtained by the linear AI/CI theory.

From the spatiotemporal point of view, the flow systems for these two cases are convectively unstable. These phenomena are also in good agreement with what was found by the linear AI/CI stability analysis (Table II).

The simulations performed for the six different cases successfully compare with the linear spatiotemporal stability results. In particular, the spatiotemporal rays, $x/t=V$, based on the propagation speeds of the left and right wave packet fronts obtained by the AI/CI theory, are still in very good agreement with the numerically obtained wave packet evolutions. It is also found that for all these cases the wave packets for the downstream and upstream modes, created by the initial pulselike disturbance, eventually separate.

We may wonder whether it is possible to find a parameter region where the unstable wave packets of the downstream and upstream modes would not be separated. For that, the velocities of the unstable wave packets for these two modes must overlap. As we know, the AI/CI boundary curves shown in Fig. 12 correspond to the zero value of the absolute growth rate, i.e., the local growth rate for an observer velocity $V=0$. Due to the symmetry of the flow system with respect to Re=0, the AI/CI boundary curves for the downstream and upstream modes intersect at Re=0. If we generalize the idea of the absolute growth rate, we can plot generalized AI/CI boundary curves for the downstream and upstream modes, corresponding to the zero value of the local

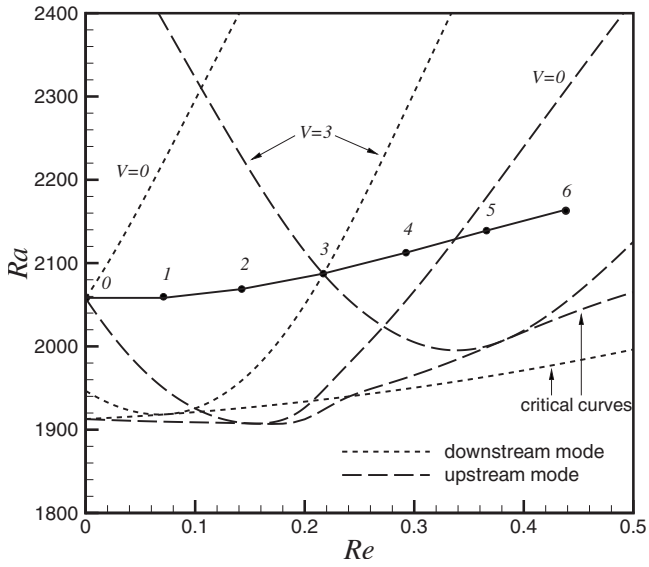


FIG. 12. Critical curves and generalized AI/CI boundary curves for different observer velocities ($V=0$ and $V=3$) in the Re-Ra plane for PRB flows with Soret effect and $\psi=-0.1$. The long-dashed curves refer to the upstream modes and the short-dashed curves refer to the downstream modes. Solid circles indicate intersection points of the generalized AI/CI boundary curves for the downstream and upstream modes for different observer velocities $V$, and the associated integers indicate the corresponding values of $V$.

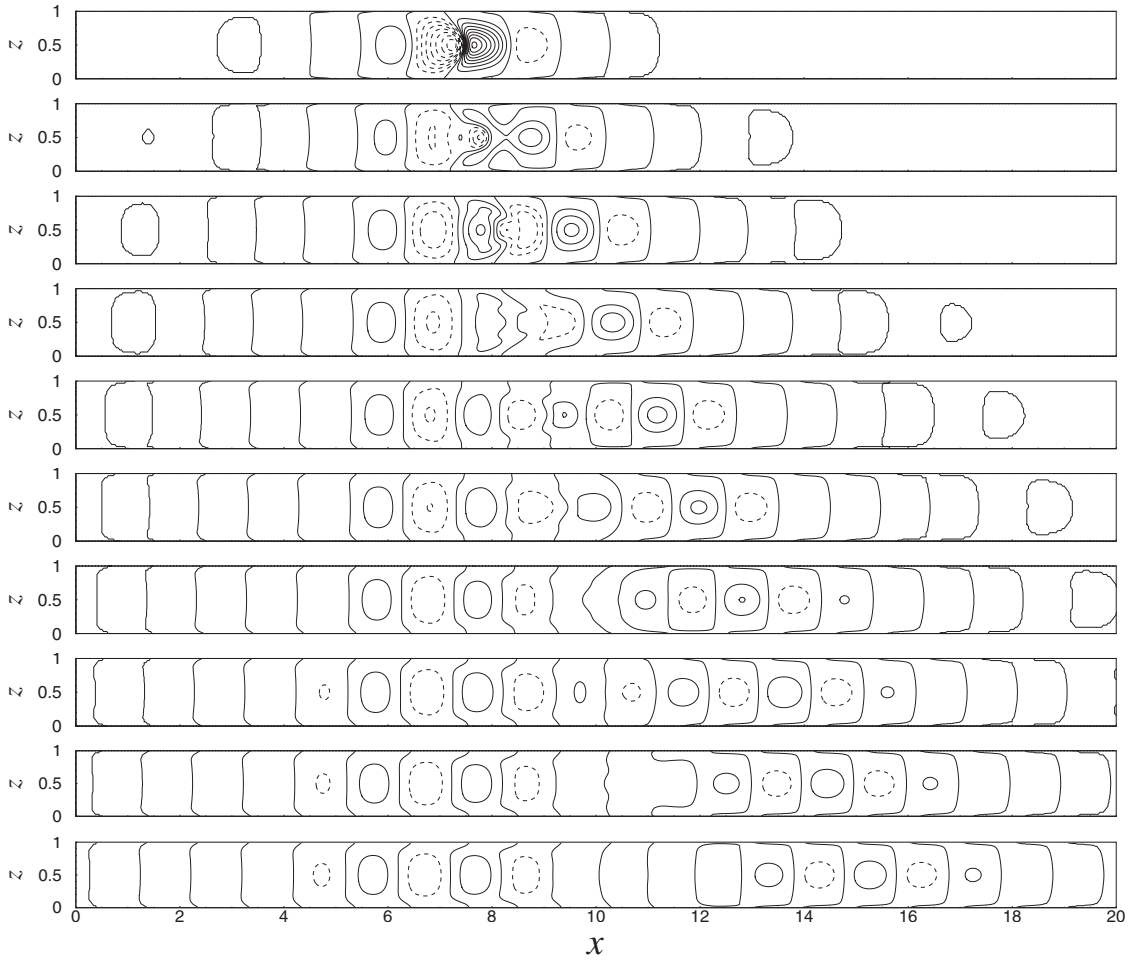


FIG. 13. Spatiotemporal patterns (concentration perturbation contours) obtained at different times ($t=n\times 0.2$ for $n=1$ to 10) in a perturbed PRB flow with Soret effect for Re=0.15, Ra=1950, and $\psi=-0.1$. In this case, the wave packets for the downstream and upstream modes eventually separate. Concerning the contours, the first solid line indicates a zero value, the other solid lines correspond to positive values and the dashed lines correspond to negative values.

growth rate for nonzero observer velocities ($V\neq 0$). For example, the generalized AI/CI boundary curves for $V=3$ are plotted in Fig. 12. From this figure, it can be seen that the generalized AI/CI boundary curve for the downstream mode has a contact point with the critical curve of the downstream mode, and similarly for the upstream mode. (For $V=0$, it was only the case for the upstream mode.) The two generalized AI/CI boundary curves intersect at a point indicated by a dot and labeled by "3," the value of $V$. Above this intersection point, there exists a parameter region which is confined by the two curves, where the unstable wave packets for the downstream and upstream modes would spread with propagation velocities in the same range around $V=3$. Furthermore, by changing the observer velocity, different pairs of generalized AI/CI boundary curves for the downstream and upstream modes can be obtained, determining a different intersection point. Thus a continuous line of intersection points can be obtained by a continuous change in the observer velocity. For the sake of simplicity, six intersection points corresponding to observer velocities equal to $V=1,2,\ldots,6$ have been calculated. These points are plotted in Fig. 12 and connected by a solid line. So, for parameters above this solid line, the unstable wave packets for the downstream and upstream modes will always overlap and no separation between them will be observed. Note also that the evolution of this overlap boundary curve with Re looks quite similar to the evolution of the critical curve for the downstream mode. The difference in Rayleigh number between the two curves is about 150 to 170. So, roughly speaking, when the temperature difference between the lower and upper plates is about 9% higher than the critical temperature difference, the separation of the unstable wave packets for the downstream and upstream modes cannot be observed.

To illustrate this, two simulations below and above the overlap boundary curve have been performed. The spatiotemporal evolutions of the concentration perturbation contours are shown in Figs. 13 and 14. The first case, which corresponds to the point b in Fig. 10 (Re=0.15, Ra=1950), is in the absolute instability region but below the overlap boundary curve, while the second case for Re=0.15 and Ra=2100 is above the overlap boundary curve. For the first case, Fig. 13 exhibits the full separation process of the wave packets for the downstream and upstream modes: after an initial amplification of the pulselike disturbance (from $t=0$ to $t=0.4$), the two wave packets which evolve with different propagation velocities [see the front velocities in Fig. 11(b)]

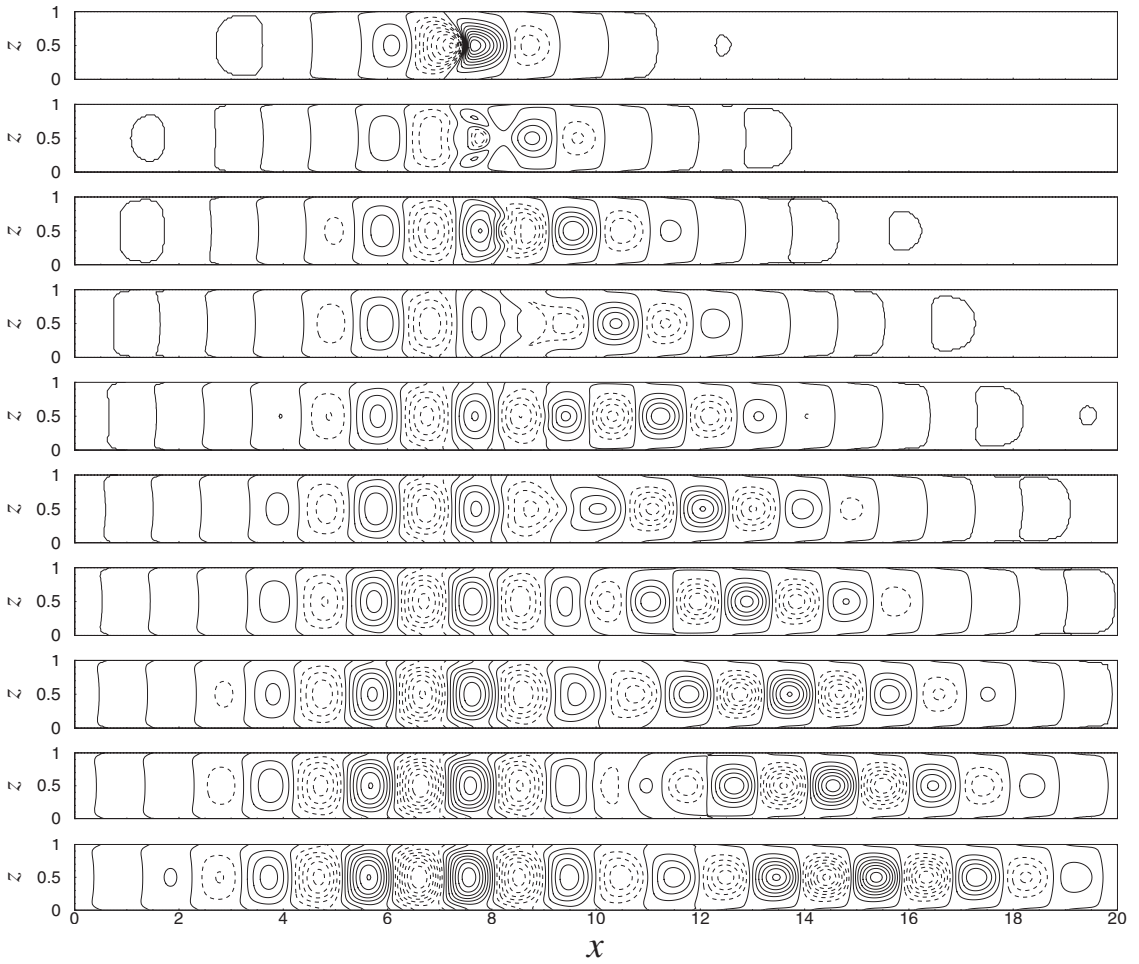


FIG. 14. Spatiotemporal patterns (concentration perturbation contours) obtained at different times ($t=n\times 0.2$ for $n=1$ to 10) in a perturbed PRB flow with Soret effect for Re=0.15, Ra=2100, and $\psi=-0.1$. In this case, the wave packets for the downstream and upstream modes never completely separate. Concerning the contours, the first solid line indicates a zero value, the other solid lines correspond to positive values and the dashed lines correspond to negative values.

begin to separate; at $t=1.8$, there exists a nearly undisturbed region between the two wave packets indicating that an almost full separation is already obtained. In contrast, for the second case, Fig. 14 shows that, although the two wave packets seem to separate, there always exists a perturbed region between them, which corresponds to an overlapping of the two wave packets. The two wave packets cannot then depart fully in this case, and the characterization of the perturbations in the overlapping region must take into account both contributions of the downstream and upstream modes. The results obtained by these simulations are in agreement with the indications given by the overlap boundary curve deduced from the linear AI/CI theory.

## V. CONCLUSION

The spatiotemporal evolution of Poiseuille-Rayleigh-Bénard flows in binary fluids with Soret effect has been investigated in this paper by nonlinear numerical simulations initiated by pulselike disturbances. The convective patterns corresponding to rolls with transverse axes are described in our two-dimensional simulations. Through selected simulations, specific behaviors revealed by the linear spatiotemporal stability analysis have been illustrated and analyzed. For positive separation factors, there exists a parameter zone in which two and even three modes with different wave numbers can coexist. The simulation shows a first case where the pulselike disturbance generates two wave packets which eventually separate, and a second case where one of the wave packets completely dominates the two others and is responsible alone for the simulated spatiotemporal evolution. For negative separation factors, different cases where the two so-called downstream and upstream modes will generate wave packets either stable, convectively unstable or absolutely unstable have been simulated. It has also been shown that there exists a boundary curve in the (Re, Ra) parameter region beyond which the wave packets of these two modes will never completely separate.

The simulations are in very good agreement with the results obtained by linear spatiotemporal stability analysis: very good comparisons are in particular obtained for the characteristics of the wave fronts and the transitions between absolute and convective instabilities when changing the parameters. It should be noticed that the initial perturbation is small enough to provide an initial growth according to a

linear mechanism. Thus the simulations can be used to directly identify the transitions between absolute and convective instabilities without the help of the linear spatiotemporal stability theory, though they need much longer computing times. Of course, the simulations are not necessarily confined to small initial conditions, and we have also used much larger initial pulselike conditions to identify the nonlinear AI/CI properties of the PRB flows (the simulated results are not presented in this paper). It is found that the nonlinear AI/CI characteristics obtained by using an initial amplitude which is thousands of times larger than that used in this paper are the same as those obtained by the linear stability theory. In other words, the fronts are linearly selected and the nonlinear effect is only confined to the intermediate region of the wave packet.

## ACKNOWLEDGMENTS

This work is supported by the Joint Fund of NSAF (Grants No. 10676005, No. 10676004, and No. 10676120), the National Natural Science Foundation of China (NSFC) (Grant No. 10702011), the Science Foundation of CAEP (Grant No. 2007B09001) and the Scientific Research Foundation for the Returned Overseas Chinese Scholars, State Education Ministry.

[1] M. C. Cross and P. C. Hohenberg, Rev. Mod. Phys. **65**, 851 (1993).
[2] C. Jung, M. Lücke, and P. Büchel, Phys. Rev. E **54**, 1510 (1996).
[3] P. Büchel and M. Lücke, Phys. Rev. E **61**, 3793 (2000).
[4] P. Büchel and M. Lücke, Phys. Rev. E **63**, 016307 (2000).
[5] D. Jung and M. Lücke, Phys. Rev. E **72**, 026307 (2005).
[6] J. Hu, H. Ben Hadid, and D. Henry, Phys. Fluids **19**, 034101 (2007).
[7] R. L. Sani, P. M. Gresho, R. L. Lee, D. F. Griffiths, and M. Engelman, Int. J. Numer. Methods Fluids **1**, 17 (1981).
[8] Y. Saad, *Iterative Methods for Sparse Linear Systems*, 2nd ed. (SIAM, Philadelphia, U.S.A., 2003).
[9] J. Hu and X. Y. Yin, Prog. Nat. Sci. **17**, 1389 (2007).
[10] I. Delbende and J. M. Chomaz, Phys. Fluids **10**, 2724 (1998).